

## LOCALIZATIONS OF THIRTEEN GAMMA-RAY BURSTS BY THE ALL-SKY MONITOR ON RXTE

D. A. SMITH<sup>1</sup>, A. M. LEVINE<sup>1</sup>, H. V. BRADT<sup>1</sup>, R. REMILLARD<sup>1</sup>, J. G. JERNIGAN<sup>2</sup>, K. C. HURLEY<sup>2</sup>,  
L. WEN<sup>1</sup>, M. BRIGGS<sup>3</sup>, T. CLINE<sup>4</sup>, E. MAZETS<sup>5</sup>, S. GOLENETSKII<sup>5</sup>, AND D. FREDERICS<sup>5</sup>

## ABSTRACT

The All-Sky Monitor (ASM) on the *Rossi X-ray Timing Explorer (RXTE)* has been used to localize thirteen confirmed X-ray counterparts to Gamma-Ray Bursts (GRBs) detected over three years of operation. We quantify the errors in ASM localizations of brief transient sources by using observations of persistent sources with well-known locations. We apply the results of this analysis to obtain accurate error boxes with reliable confidence levels for the thirteen GRBs. In six of these thirteen cases, multiple detections by the ASM allow the positions to be localized to a diamond of order  $\sim 15' \times 3'$ . In five further cases, the Interplanetary Network (IPN) constrains the usually  $\sim 3^\circ \times 3'$  (full-width) ASM error box to an area of a few tens of square arcminutes. This work adds eleven burst localizations to the list of  $\sim 60$  well-localized GRBs.

*Subject headings:* gamma rays: bursts

## 1. INTRODUCTION

The recent achievement of fast, accurate localizations of Gamma-Ray Bursts (GRBs) has led to great progress in the study of these enigmatic events. The Wide-Field Camera (WFC) on *BeppoSAX* (Jager et al. 1998) was used to localize the X-ray flash associated with GRB 970228 within a circle  $3'$  in radius (Costa et al. 1997a). Eight hours later this circle was imaged with the *BeppoSAX* Narrow-Field Instruments, and a fading X-ray source was found and localized to within a circle of  $50''$  in radius (Costa et al. 1997b). The location of the fading source was consistent with the WFC position. Both of these positions were widely disseminated among the astronomical community within a few hours, and led to a cascade of reports in the IAU Circulars (25 Circulars between Nos. 6572 and 6747), including the first report of a detection of an optical counterpart to a GRB source (van Paradijs et al. 1997).

Since GRB 970228 was localized and identified, the WFC has been used to provide rapid, accurate positions for almost twenty further GRBs, and many of these positions have led to significant advances in the understanding of GRBs. The early successes of the *BeppoSAX* GRB localization program also motivated other successful projects to use X-ray emission to rapidly localize GRBs, such as the work reported on in this paper and the efforts reported by Takeshima et al. (1998). These X-ray localizations have led to identifications of GRB source counterparts in many wavebands, enabling scientists to learn more about their locations, properties, and behavior. Optical spectroscopy of the fading counterparts of GRB sources and what are thought to be their host galaxies has led to the determination of five precise cosmological redshifts at the time of this writing (perhaps six – GRB 980425 may be a special case: see Kulkarni et al. 1998b). GRB 970508 was found to have a redshift  $z \gtrsim 0.83$  (Metzger et al. 1997), the host galaxy for GRB 971214 was measured at  $z = 3.4$  (Kulkarni et al. 1998a), and the host for GRB 980613 shows an emission line at  $z = 1.0964 \pm 0.0003$  (Djorgovski et al. 1999). The counterpart to GRB 980703 displayed emission and ab-

sorption features at  $z = 0.965$  (Djorgovski et al. 1998), and the spectrum of GRB 990123 showed many absorption features at  $z = 1.600 \pm 0.001$  (Kelson et al. 1999; Hjorth et al. 1999). This is a rapidly-changing field, and new discoveries are reported almost monthly, but these measurements indicate that at least some GRB sources are at cosmological distances.

The observations of the temporal variation of the emission from a GRB source in many spectral bands has made it possible to infer physical parameters of the underlying explosive event (Wijers & Galama 1998) according to the relativistic fireball model (Rees & Mészáros 1992). Further progress in all areas of GRB investigation now depends primarily on the rapid and accurate determination of the positions of more GRBs, so as to quickly bring the source positions under the scrutiny of powerful X-ray, optical, and radio telescopes.

The All-Sky Monitor (ASM) on the *Rossi X-ray Timing Explorer (RXTE)* continually scans the sky in the 1.5–12 keV band (Levine et al. 1996). Like the *BeppoSAX* WFC, it uses a proportional counter to measure the X-ray shadows of a coded-mask, to thereby obtain fine angular resolution over a wide field of view. Although the design of the ASM was not optimized to perform studies of GRB sources, on occasion it serendipitously observes the X-ray component of a GRB. Such observations can be used to obtain the precise position of the GRB source soon after the event. The schedule of ASM observations is determined in advance and is never adapted to respond to alerts from other instruments.

Real-time monitoring of ASM data from May 1997 to January 1999 has led to the detection and rapid localization of six GRBs. A search of archival data has revealed that at least eight GRB events were detected with the ASM in the first eighteen months of its operation, although GRB 961216 could not be reliably localized. Of the thirteen GRBs localized by the ASM, only one, GRB 971214, was also detected by the *BeppoSAX* WFC. In this paper we report the celestial positions of the ASM-detected GRB events, and we describe the capabilities of the ASM to localize brief X-ray transients.

<sup>1</sup>Center for Space Research and Department of Physics, MIT, Cambridge, MA 02139

<sup>2</sup>Space Sciences Laboratory, University of California, Berkeley, CA 94720-7450

<sup>3</sup>NASA/MSFC, Code ES-84, Huntsville, AL 35812

<sup>4</sup>NASA Goddard Space Flight Center, Code 661, Greenbelt, MD 20771

<sup>5</sup>A. F. Ioffe Physico-Technical Institute, Politechnicheskaya 26, 194021 St. Petersburg, Russia

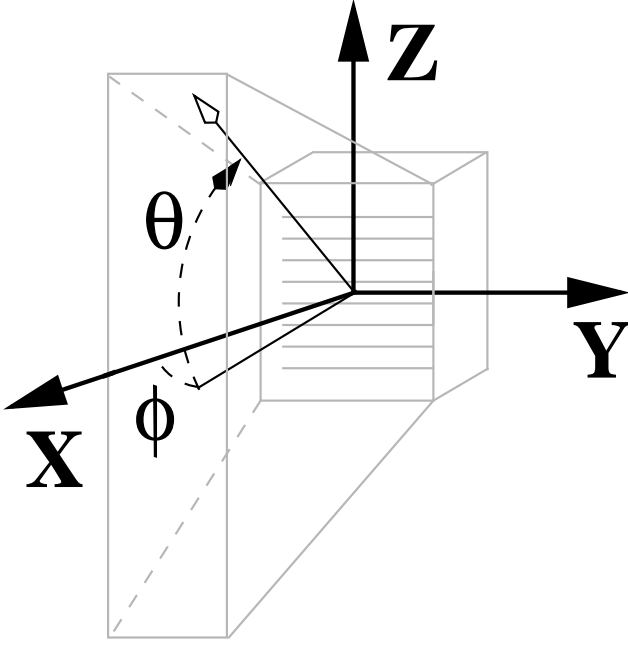


Fig. 1 – This diagram defines a Cartesian coordinate system and associated angles used to describe positions and directions relative to a particular SSC. The coordinate axes are superposed upon a schematic drawing of an SSC which represents the outer shell of the collimator and the proportional counter. The eight parallel lines within the counter represent the resistive anodes which are used to obtain the  $y$  coordinates of detected events. The origin of the coordinate system is located at the center of the window of the proportional counter. The  $x$ -axis extends through the center of the coded mask so as to point in the direction of the center of the field of view of the SSC. The  $y$ -axis points parallel to the resistive anodes, and the  $z$ -axis points parallel to the long axis of the mask slits. A direction relative to the SSC may be specified by the angles  $\phi$  and  $\theta$ , where  $\phi$  is measured in the  $x$ - $y$  plane and  $\theta$  is the angle between the  $x$ - $y$  plane and the specified direction. The field of view of the SSC extends over a region defined by  $-6^\circ \leq \phi \leq +6^\circ$  and  $-55^\circ \leq \theta \leq +55^\circ$  (FWZI). Note that each of the three SSCs has a unique orientation on the ASM (see Figure 1 of Levine et al. 1996).

## 2. ASM SOURCE POSITION ANALYSIS

### 2.1. Instrumentation and Analysis

The ASM consists of three Scanning Shadow Cameras (SSCs) mounted on a motorized rotation drive. The assembly holding the three SSCs is generally held stationary for a 90-s “dwell”. The drive then rotates the SSCs through  $6^\circ$  between dwells, except when it is necessary to rewind the assembly. Each SSC contains a proportional counter with eight resistive anodes. Each event detected on exactly one resistive anode is characterized by SSC and anode numbers, total pulse height, and a one-dimensional position in the coordinate parallel to the anode, determined via the charge-division technique. Each SSC views a  $12^\circ \times 110^\circ$  (FWZI) field through a mask perforated with pseudo-randomly spaced slits. The long axes of the slits run perpendicular to the anodes.

For each dwell, the intensities of known sources in the field of view (FOV) are derived via a fit of model slit-mask shadow patterns to histograms of counts as a function of position in the detector. The residuals from this fit are then cross-correlated with each of the expected shadow patterns corresponding to one of a set of possible source directions which make up a grid covering the FOV. A peak in the resulting cross-correlation map indicates the possible presence and approximate location of a new, uncataloged X-ray source. Peaks that satisfy certain criteria are analyzed further to confirm the detection and refine the position. For detections of bright sources, the resulting error boxes typically have sizes on the order of  $3' \times 3^\circ$  full width at 90% confidence. Detections of new sources in at least two SSCs are preferred because they yield error boxes that cross, thereby constraining the source’s location in two dimensions to a diamond-shaped error box, of dimensions  $\sim 3' \times 15'$  for bright sources.

Errors in the model of the shadow patterns from known sources in the FOV can lead to “ripples” in the cross-correlation map which act as a source of noise in addition to counting statistics. The correct construction of the shadow patterns depends on an accurate calibration of the correspondence between electrical position, which is directly derived via application of the charge-division technique, and physical location within the detector. The electrical position - physical location correspondence in the SSCs is drifting with time as the carbon coating of the resistive anodes is being worn away nonuniformly. We therefore periodically update our calibration of this correspondence.

### 2.2. The Error Distributions

For a GRB source position, it is essential to report an accurate error box with a reliable confidence level, i.e., a good estimate of the probability that the source is within the box. In this section, we describe our method of determining the association between error box size and confidence level. The method is empirical and relies on observations of persistent X-ray sources. If a source is removed from the catalog of known sources used in the initial fit, it functions as a new source to be detected and localized with our standard software. The derived location may then be compared with the known precise location of that source’s optical counterpart.

This procedure was performed on 13,982 observations of six X-ray sources, chosen to provide a wide range of intensities (Table 1). We chose the test observations from five 50-d time intervals when the six test sources were observed most often. The best-fit position from each observation of one of the six sources was compared with the catalogued source position to obtain deviations in both FOV coordinates,  $\phi$  and  $\theta$  (Fig. 1). The distribution of the resulting position errors provides the basis for the association between confidence levels and error box sizes (Fig. 2).

There are four main characteristics of an observation that can affect the accuracy of attempts to localize a source within that observation: the source’s intrinsic brightness, the source’s FOV location, the contribution to the background from other sources in the FOV, and the number of diffuse background counts. One advantage to the coded-mask imaging technique is that the background strength to which the signal strength should be compared is not the total number of non-signal counts in the

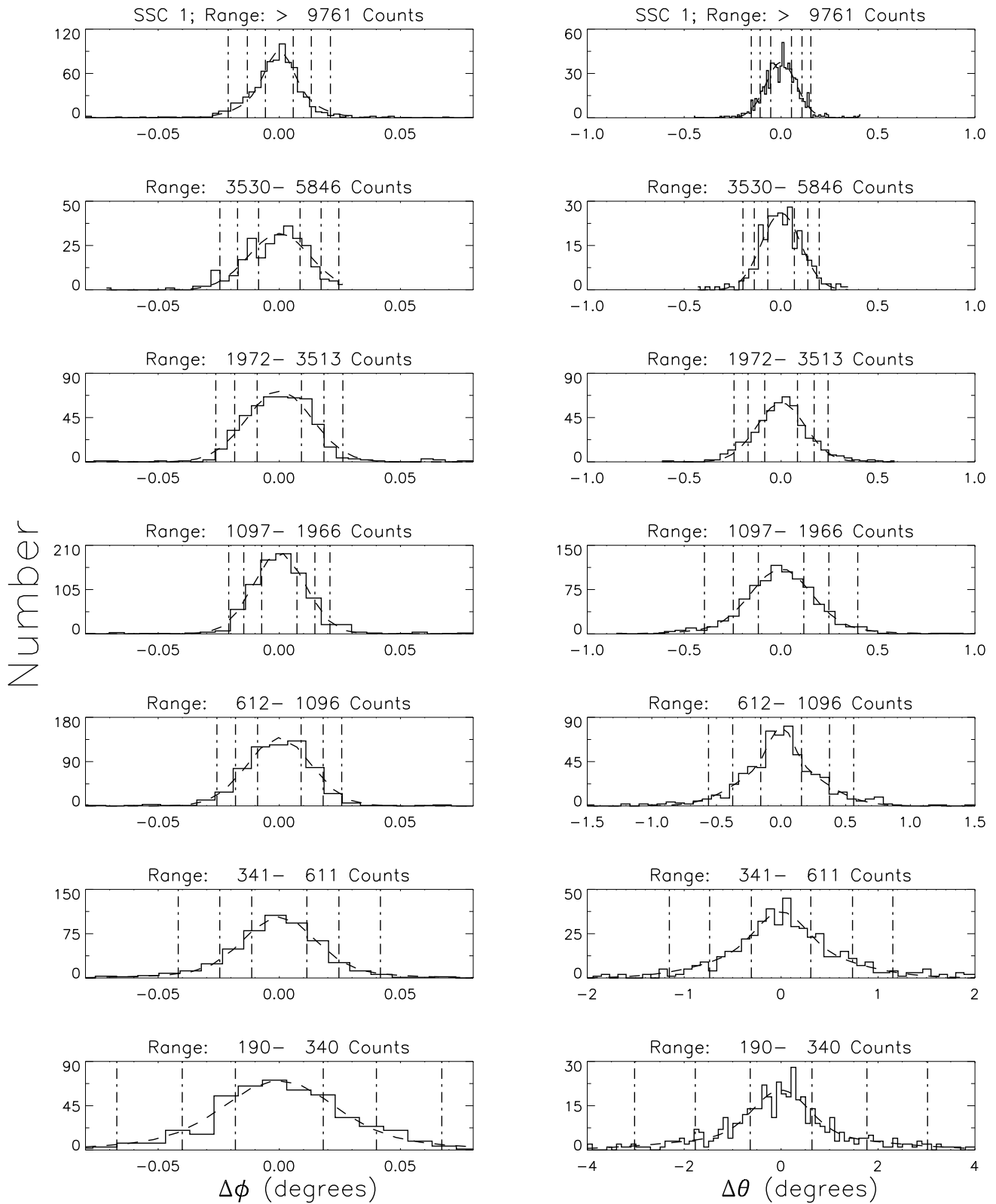


Fig. 2.— A demonstration of the position-determining ability of SSC 1 and the validity of the model used to calculate confidence limits. Each histogram shows the distribution of errors in  $\phi$  (left panels) and  $\theta$  (right panels) between the derived source position and the actual celestial position for detections of sources with measured source counts within a certain range. The number of counts increases vertically in the figure. Note that the abscissa scale is not the same in each panel. The dashed curve represents the best-fit model of two summed Gaussian curves and a constant term to these data. The presence of the constant term is not obvious, because the abscissa scale is defined to emphasize the central peak. Broken vertical lines indicate the symmetric zones containing 50%, 82% and 95% of the area under the double-Gaussian curve.

TABLE 1  
CALIBRATION SOURCES

Source Name	R.A. (J2000)	Decl. (J2000)	Intensity (mCrab) <sup>a</sup>	No. in SSC 1 <sup>b</sup>	No. in SSC 2 <sup>b</sup>	No. in SSC 3 <sup>b</sup>
Sco X-1	16h 19m 55.13s	-15°38'24.4"	9000-23000	755	816	1153
Crab	05h 34m 31.97s	+22°00'52.2"	930-1100 <sup>c</sup>	598	546	1644
Cyg X-2	21h 44m 40.97s	+38°19'18.1"	200-900	1148	1151	353
Cyg X-3	20h 32m 25.54s	+40°57'27.7"	70-600	1378	1368	400
Her X-1	16h 57m 49.73s	+35°20'32.3"	< 200	222	218	44
X 0614+091	06h 17m 7.32s	+09°08'13.6"	< 200	416	293	300

<sup>a</sup>Intensity in mCrab derived from detected count rates, adjusted to simulate observations with the source at the center of the FOV of SSC 1, and normalized to a nominal count rate of 75 c/s for the Crab Nebula at the center of the FOV of SSC 1.

<sup>b</sup>The number of observations of each source used to analyze the position error.

<sup>c</sup>Including statistical and systematic errors in ASM detections.

entire detector, but rather the number of non-signal counts detected in that portion of the detector which is illuminated by the (off-axis) source of interest.

The dominant contribution to the total background is usually from diffuse celestial X-ray emission for which  $\sim 2500$  counts are typically detected per observation. A relatively small number of counts,  $\sim 150$ – $450$ , are contributed from non-X-ray background. Occasionally, substantial fluxes of solar X-rays scattered in the Earth’s atmosphere or the inside surface of the one of the collimators are detected. This solar X-ray contamination can contribute up to  $\sim 1600$  counts to the total background. For the  $\sim 14,000$  observations used in this analysis, the median number of counts in a single SSC per dwell (excluding the counts from the test source) is  $\sim 3150$  (1.5–12 keV). Only  $\sim 20\%$  of the observations had a total background higher than 5000 counts, and only  $\sim 5\%$  of the observations had more than 9750 background counts. Half of the observations show a total background between 2000 and 4000 counts, indicating that there were no other strong discrete sources in the FOV besides the test source.

Observations that have more than about 4000 total background counts most often have other point X-ray sources in the FOV. These other sources can increase the statistical noise in an observation, as well as the likelihood for systematic errors in a derived position. However, the effect of a widely separated source on the derived position for the test source tends to be small, since the overlap between the shadow patterns of such sources is generally small. To minimize the effect of other sources on our results, the six test sources were selected in part because they are relatively isolated on the sky. Only two of these six sources are within  $15^\circ$  of another X-ray source bright enough to be detected by the ASM. The smallest separation is the  $\sim 9^\circ$  separation of Cyg X-3 from Cyg X-1. In the case of Sco X-1, nearby Galactic plane sources contribute significantly to the total background, and indeed, Sco X-1 is the test source in 73% of the 1271 observations that have more than 8000 total background counts. However, Sco X-1 is so bright (an on-axis, 90-s observation typically yields more than 68,000 counts) that contamination by these sources is not expected to have any sig-

nificant effect on the localization accuracy. We therefore did not expect, *a priori*, that the presence of other sources in the FOV would often have a large effect upon the local statistical noise at the positions of the test sources.

If the counts from other sources are not properly modeled and subtracted via the initial fit, the noise level near the test source may be enhanced by systematic “ripples” in the cross-correlation map, even if the sources are well-separated in the FOV. To minimize these ripples, the calibrated relations between electrical position and physical location at a time near the middle of each interval were used in the generation of the model shadow patterns used to fit observations taken during that interval. The use of *a posteriori* calibration ensures that the detector response will be modeled as accurately as possible, which means not only that the test sources will be localized as accurately as possible, but that other discrete X-ray sources will have a minimal effect on systematic noise near the source of interest. For real-time operations, we generate model shadow patterns based on an extrapolation of the two most recent calibration measurements. Over months, the true calibration will drift from this set of extrapolated values, degrading the localization accuracy and increasing the systematic noise. We therefore update the calibration periodically, but there may be times when the localization accuracy in real-time operations will not achieve the level presented here.

We parameterize the position error as a function of the total number of counts observed from a source during a single observation. The collimator reduces the area of the detector exposed to an off-axis source, so that sources of the same intrinsic brightness will yield different numbers of counts if they are observed at different locations in the FOV. For example, a  $\sim 300$  mCrab source at the center of the FOV will generate  $\sim 2000$  counts in a 90-s observation, while the same source at  $\phi = \pm 4.0^\circ$  will only contribute  $\sim 700$  counts. The FOV position of the relevant test source is effectively random. Thus, the 14,000 test observations yield numbers of source counts that span the entire range expected from a single source during a

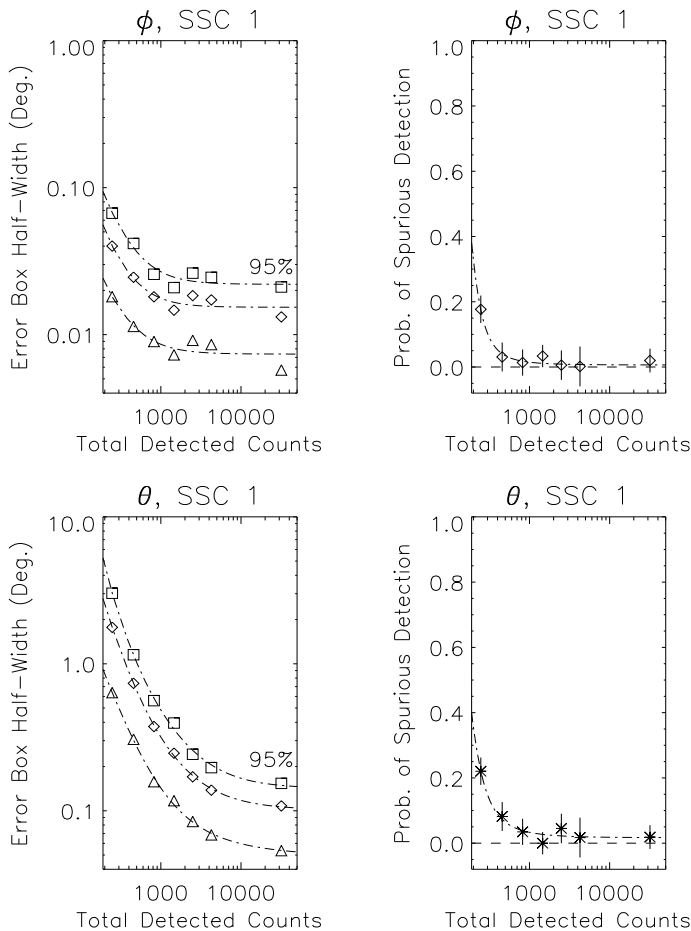


Fig. 3 – The functions used to set the size of the ASM error box for a new X-ray source observed by SSC 1. The left panels display the half-widths of error boxes in each of two dimensions at three levels of confidence (95%, 82%, and 50%), as modeled by the two-Gaussian model for the histograms shown in Figure 2. The right panels display the fraction of the measurements unaccounted for by that model, which we assume to be noise peaks mistaken for sources. All graphs use the total measured counts from the source as the abscissa.

### 90-s ASM dwell.

For this analysis, we assume that an off-axis bright source and an on-axis dim source that both yield the same number of counts in an observation can be localized with approximately the same accuracy. The off-axis source illuminates the detector through fewer mask slits, yielding fewer shadow edges in the position histograms that can be used to localize the source in the cross-correlation process. However, each slit edge will be defined by a greater count rate contrast, and the effective number of background counts will be reduced in proportion to the reduction in the exposed area of the detector. If the localization accuracy were to scale like the detection sensitivity, we would expect it to be approximately inversely proportional to the square root of the exposed fraction of the FOV, if the numbers of source and background counts are held constant. Therefore, over a restricted region of the FOV, any error in estimating error box sizes using the number of source counts rather than a more sophisticated estimator is expected to be limited. For sources near the edge of the FOV, this approximation is poor and calibration errors have a particularly large effect, so we only consider observations where the test source was located

such that  $|\phi| < 4.6^\circ$  or  $|\theta| < 45^\circ$ .

We checked whether the effects of the test sources' FOV locations are adequately approximated by our assumption that the localization accuracy depends only on the number of source counts. To do this, we separated the  $\sim 14,000$  observations into two groups according to the  $\phi$  coordinate of the test source's actual location, i.e., the two groups were defined by  $|\phi| < 2.0^\circ$  and  $2.0^\circ \leq |\phi| \leq 4.6^\circ$ . We binned the deviations between the actual and derived source locations according to number of source counts and FOV group and obtained two sets of error histograms. The widths of the resulting error distributions for either the  $\theta$  or  $\phi$  coordinate did not show any clear systematic dependence on FOV group.

The effect of the background level on the accuracy of our localizations was similarly checked by dividing the set of observations into groups based on the total background, i.e., all counts excluding those from the test source. We again calculated position error distributions based on test source counts for each of these groups. The error distributions for the high background cases ( $> 4000$  counts) were found to be indistinguishable within statistical limits from the distributions for the low background cases ( $< 4000$  counts). The cases in which the number of total background counts rose above 8000 were also examined. As noted, 73% of these observations used Sco X-1 as the test source. No significant difference between the error distributions from these observations with high total background and those of low total background was found. These results indicate that sources widely separated from the test source have only small effects on the localization of the test source. A new source that appears close to a strong source will not be localized as accurately as indicated by the present results, but we have not tried to quantify the effects of other nearby sources.

We therefore proceed as follows: for each of the  $\sim 14,000$  observations we record both the total number of photons detected from the test source and the deviation of the derived position in  $\phi$  and  $\theta$  from the true position. We separate the location measurements according to the number of detected source counts into seven groups per SSC and bin the angular errors for all observations in each group into histograms. Figure 2 shows the resulting distributions for SSC 1. The equivalent histograms for the other two SSCs look similar.

### 2.3. A Model for the Error Boxes

We modeled each histogram of coordinate errors as the sum of a narrow Gaussian, a wide Gaussian, and a constant. For bright sources, a single narrow Gaussian is sufficient to obtain a reasonable fit. For small values of source counts, there is a significant chance that noise in the cross-correlation map will result in an incorrect identification of the source location. The noise may raise a side lobe of the instrument response to a value higher than the peak at the source location. This yields broad wings on the side of the central peak in the error histograms. These wings are modeled by the wide Gaussian. Noise peaks may even exceed the value of any response to the test source, which results in a population of measured errors that are distributed uniformly across the whole range of allowed values for each angle. This uniform scatter is present but not obvious in Figure 2, because only the region near the central peak is displayed. At extremely low source counts, the central Gaussian peak disappears entirely, leaving only the random scatter. There is no evidence for a central peak below  $\sim 200$  counts in SSCs 1 and 2 and below  $\sim 300$  counts in SSC 3.

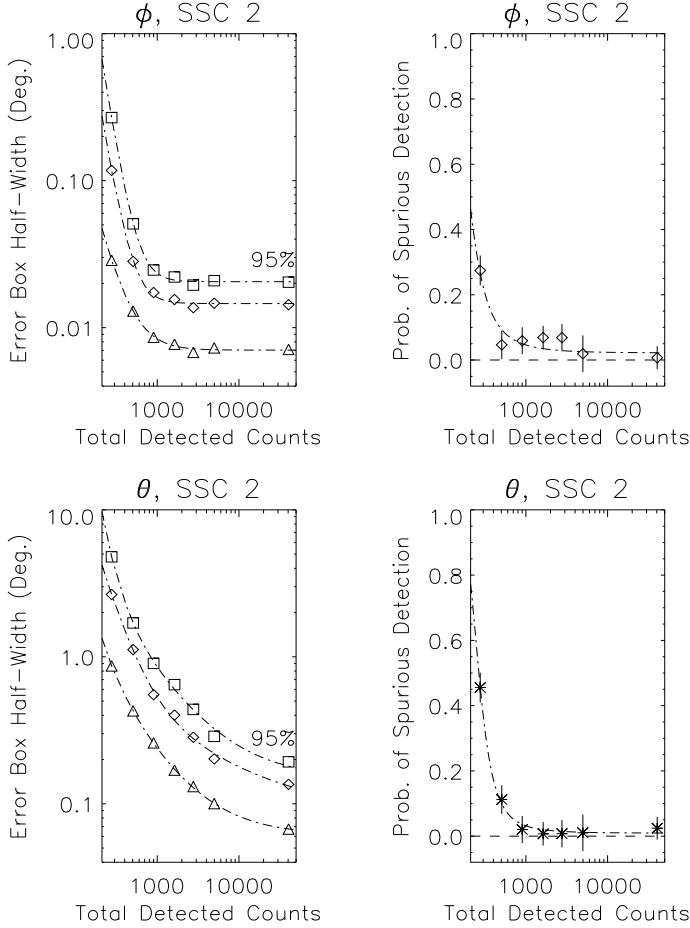


Fig. 4 – The functions used to set the size of the ASM error box for a new X-ray source observed by SSC 2. See caption for Figure 3.

Our strategy in reporting error boxes is to define uncertainties in each FOV coordinate appropriate to a given confidence level under the assumption that the detection was of a real source. In addition, we quote the probability that the detection was spurious. The estimated probabilities are derived by integrating under the components of the best-fit model distribution. A confidence interval at  $x\%$  is defined as the symmetric interval about zero such that the integral of the two Gaussian curves over that interval yields  $x\%$  of the integral of the same Gaussians over the entire range of possible errors. Figure 2 displays as vertical broken lines the values in both the  $\phi$  and  $\theta$  directions that correspond to 50%, 82% and 95% confidence limits for SSC 1.

The uncertainty in each coordinate associated with each of the selected confidence limits is plotted as a function of the number of detected source counts in the left panels of Figures 3–5. We used these results to derive interpolation functions which give FOV coordinate uncertainties for the source location at three significance levels for any number of source counts. We chose as an interpolation function the sum of two power laws and a constant. The constant represents the limiting systematic error (with values of  $\sim 1.5'$  in  $\phi$  and  $12'$  in  $\theta$  at 95% confidence), and the power laws are simply a convenient means to interpolate between the estimated angular uncertainties. The best-fit interpolation functions are graphed as broken lines in the left panels of Figures 3–5.

The difference between the total number of measurements in the histogram and the area under the two model Gaussian

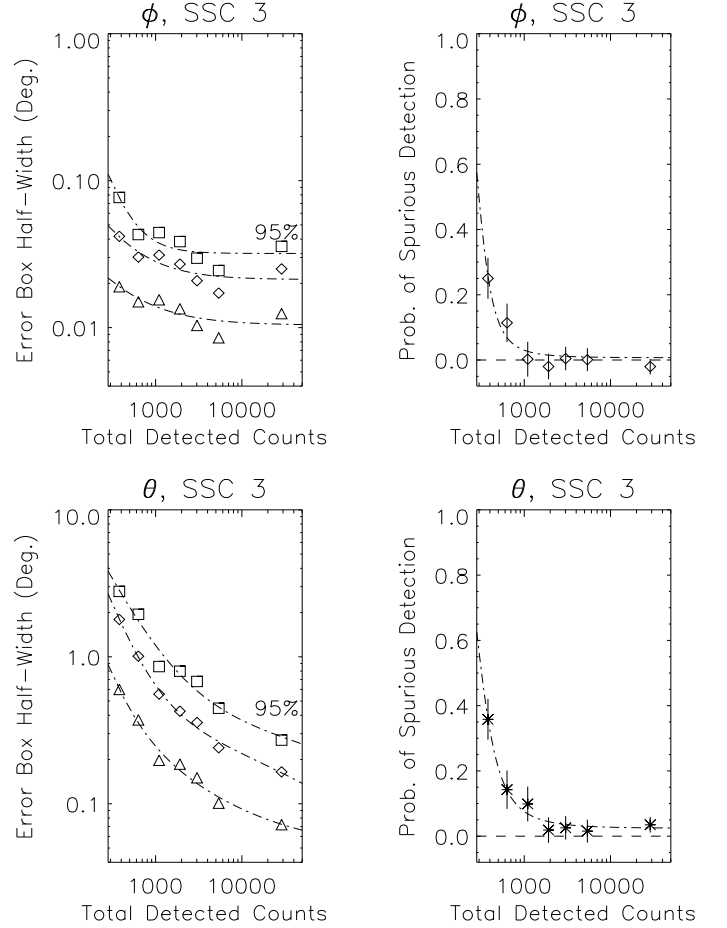


Fig. 5 – The functions used to set the size of the ASM error box for a new X-ray source observed by SSC 3. See caption for Figure 3.

curves is a measurement of the probability of mistaking a noise peak for the source. This difference is plotted in the right panels of Figures 3–5. The error bars reflect the counting statistics of the total number of actual measurements in each histogram, and are typically 3–7%. These figures show that the probability of misidentifying a source increases as the number of detected photons decreases. To interpolate between these points, we use the formula:

$$f(x) = \frac{1.0}{1 + e^{-b/(x-a)}} \quad (1)$$

where  $x$  is the number of detected source counts, and  $a$  and  $b$  are constant parameters determined by a least-squares fitting procedure. We chose this function because it could match the rising behavior of the data at low numbers of counts, while also ensuring that the probability never exceeded one or dropped below zero. The best-fit functions are plotted as broken lines in the right panels of Figures 3–5. Note that extrapolation of this function below the 200–300 count limit mentioned above is not meaningful.

It is our practice to define error box sizes based on the double-Gaussian integration limits (left panels; Figs. 3–5) and to separately specify the probability that the detection is spurious (right panels; Figs. 3–5). The former yield a probability  $p$  ( $= 0.95, 0.82$  or  $0.50$ ) that the actual GRB location lies within the associated interval. There is a probability of  $p^2$  that the actual GRB location lies within two of these intervals. A box on the sky, defined by 95% limits in each of two directions, is

TABLE 2  
PROPERTIES OF 13 ASM-DETECTED GRBS

Date of GRB (yymmdd)	Time of GRB (hh:mm:ss)	Confirming Satellite <sup>a</sup>	2-12 keV Fluence ( $10^{-7}$ ergs $\text{cm}^{-2}$ )	R.A. (J2000)	Decl. (J2000)
960416	04:58:59	ub	$6.0 \pm 0.3$	04h15m27s	+77°10'
960529	05:34:34	k	$> 17.5 \pm 0.6$	02h21m50s	+83°24'
960727	11:57:36	uk	$9.5 \pm 0.5$	03h36m36s	+27°26'
961002	20:53:55	uk	$9.2 \pm 0.5$	05h34m46s	-16°44'
961019	21:08:11	ub	$4.6 \pm 0.6$	22h49m00s	-80°08'
961029	19:05:10	k	$3.3 \pm 0.4$	06h29m27s	-41°32'
961230	02:04:52	u	$1.5 \pm 0.3$	20h36m45s	-69°06'
970815	12:07:04	ubks	$> 33.3 \pm 0.8$	16h08m33s	+81°30'
970828	17:44:37	ub	$> 14.9 \pm 0.6$	18h08m23s	+59°19'
971024	11:33:32	b	$1.1 \pm 0.3$	18h25m00s	+49°27'
971214	23:20:41	ubks	$3.4 \pm 0.3$	12h04m56s	+64°43'
980703	04:22:45	ub	$> 18.3 \pm 0.8$	23h59m04s	+08°33'
981220	21:52:21	uks	$12.6 \pm 0.5$	03h43m38m	+17°13'

<sup>a</sup>u - *Ulysses*; b - BATSE; k - KONUS; s - *BeppoSAX*

therefore a 90% confidence region. In the case of a single-SSC detection, the two intervals will be in terms of  $\phi$  and  $\theta$  in that SSC, but if detections of a given source are available in two SSCs, the diamond formed by the intersection of the two  $\phi$  intervals can be taken as the 90% region (See Figure 6). Similarly, using the 82% values in each direction will yield an error box at 68% confidence, and the 50% values will yield a joint error box at 25% confidence. In cases of weak source detections, this smallest box helps illustrate the deviations of the actual error distributions from simple Gaussians.

We have thus derived functions to estimate source position uncertainties corresponding to the 95%, 82%, and 50% confidence limits in each of two dimensions, valid for detections of more than 200-300 counts under the assumption that the corresponding peak in the cross-correlation map represents a valid source detection. We find that the width of the error distribution can be effectively parameterized as a function of the total number of counts detected from a source. This analysis is valid for the central region of the FOV, when the sky around the new source is free of contaminating sources, and an accurate calibration of the electrical-physical position correspondence in the detector is available. Under these conditions (which may not hold for all real-time detections), this analysis provides a rational means for associating error-box sizes with confidence levels.

### 3. RESULTS

In this paper, we report the positions of thirteen Gamma-Ray Bursts (GRBs) localized with the ASM in its first three years of operation. It is impossible to unambiguously distinguish a GRB from an X-ray burst on the basis of ASM data alone. We therefore report the positions of thirteen events which have been identified as GRBs through the comparison of ASM timing and location information with data from other operational GRB detectors including BATSE on the *Compton Gamma Ray Observatory*, the Gamma-Ray Burst Instrument on

*Ulysses*, KONUS on the *Wind* spacecraft, and the Gamma-Ray Burst Monitor on *BeppoSAX* (See Table 2). These instruments, as well as the Interplanetary Network (IPN) triangulation technique, are described elsewhere (See, e.g. Fishman et al. 1995; Hurley et al. 1999a, b; Briggs et al. 1999; the IPN web site <http://ssl.berkeley.edu/ipn3/>).

Pertinent data on these thirteen bursts are given in Tables 2–6. Table 2 gives the onset times, 1.5–12 keV fluences, and centers of the ASM error boxes, Table 3 gives the error box sizes and position angles for the single-SSC detections, and Table 4 gives the celestial coordinates of the corners of the best intersection diamonds in cases of two-SSC detections. Table 5 reports the circular localizations achieved with other high-energy instruments, while Table 6 describes the available IPN annuli.

The GRBs described in this paper were discovered through the use of four different techniques. First, we searched the ASM data at the approximate times and rough locations (the radii of the error circles were not available at the time of our search) of 438 GRBs determined from BATSE data between 1996 Jan 6 and 1997 Jul 15 (see, e.g., <http://www.batse.msfc.nasa.gov/data/grb/catalog/> for times and locations). If the trigger time of a burst corresponded to a time when the ASM was collecting data, and if the BATSE localization was within the ASM FOV at that time, the relevant ASM observation was searched for evidence of a GRB detection. This search resulted in the discovery of X-ray counterparts for GRB 960416 (Figure 6a) and GRB 961019 (Figure 6e). The former event was detected by two SSCs simultaneously, while the latter was only detected by SSC 2. Both events were also detected by the *Ulysses* GRB instrument, so IPN annuli could be calculated. Both annuli were consistent with the ASM positions, and in the case of GRB 961019, the IPN annulus reduced the length of the error box to 11'.

Second, we searched through the ASM time-series data up to September 1997 for episodes of transient emission that could be from GRBs not detected by BATSE. We performed linear

TABLE 3  
PROPERTIES OF SINGLE-SSC ASM ERROR BOXES

Date of GRB (yymmdd)	Length (arcmin.)	Width (arcmin.)	Position Ang. <sup>a</sup> (deg.)
960727	65.4	2.5	51.85
961002	76.3	2.6	82.19
961019	493.2	25.6	52.34
961029	522.5	28.0	-54.71
971024	249.5	6.5	64.38
971214	204.2	5.7	-62.54
981220	58.9	2.5	75.64

<sup>a</sup>Defined such that positive is east of north.

TABLE 4  
CORNERS OF MULTIPLE-SSC ERROR BOXES

Date of GRB (yymmdd)	R.A. 1 Decl. 1 (J2000)	R.A. 2 Decl. 2 (J2000)	R.A. 3 Decl. 3 (J2000)	R.A. 4 Decl. 4 (J2000)
960416	04h15m32.8s +77°11'17"	04h13m30.0s +77°07'20"	04h15m21.9s +77°08'00"	04h17m25.4s +77°11'54"
960529	02h21m19.8s +83°25'33"	02h19m57.3s +83°18'07"	02h22m17.3s +83°22'38"	02h23m43.3s +83°30'03"
961230	20h37m25.6s -68°58'27"	20h36m34.9s -68°44'07"	20h35m58.9s -69°13'09"	20h36m50.3s -69°27'29"
970815	16h08m18.7s +81°32'00"	16h06m16.7s +81°27'14"	16h08m47.1s +81°29'32"	16h10m51.1s +81°34'15"
970828	18h08m42.4s +59°19'33"	18h07m58.6s +59°18'08"	18h08m36.9s +59°17'00"	18h09m20.7s +59°18'25"
980703	23h59m07.0s +08°32'05"	23h59m23.3s +08°38'01"	23h59m02.0s +08°34'43"	23h58m45.7s +08°28'47"

TABLE 5  
SIZES OF ERROR CIRCLES

Date of GRB (yymmdd)	Instrument	R.A. of Center (J2000)	Decl. of Center (J2000)	Radius (Degrees)
960416	BATSE	04h27m24s	+73°36'0"	4.8
961019	BATSE	21h27m29s	−84°10'50"	5.0
970815	BATSE	15h37m58s	+81°42'0"	4.0
970815	ASCA	16h06m54s	+81°30'34"	0.0167 <sup>a</sup>
970828	BATSE	17h56m53s	+59°25'10"	4.8
970828	ASCA	18h08m30s	+59°19'20"	0.025 <sup>b</sup>
970828	ROSAT	18h08m31.7s	+59°18'50"	0.00278 <sup>c</sup>
971024	BATSE	18h01m53s	+49°38'20"	6.9
971214	BATSE	12h03m19s	+66°12'40"	4.1
971214	BeppoSAX - WFC	11h56m30s	+65°12.0'	0.065 <sup>d</sup>
971214	BeppoSAX - NFI	11h56m25s	+65°13'11"	0.0167 <sup>e</sup>
980703	BATSE	23h56m17s	+12°00'40"	4.0
980703	BeppoSAX - NFI	23h59m07s	+08°35'33"	0.0139 <sup>f</sup>

REFERENCES.—a - Murakami et al. 1997a; b - Murakami et al. 1997b; c - Greiner et al. 1997; d - Heise et al. 1997; e - Antonelli et al. 1997; f - Galama et al. 1998

least-squares fits to the count rates for each 90-s dwell of the ASM. Steady or very slowly changing count rates (on time-scales between 1/8 and 90 s) yielded low values of  $\chi^2$ . We then examined the observations yielding the highest values of  $\chi^2$  for GRB-like events. We excluded cases where a bright, persistent source moved in or out of Earth occultation or a known highly variable source like GRS 1915+105 was in the FOV. We searched the position data from the remaining dwells for indications of new sources. Observations containing a new source candidate with an intensity measurement of  $5\sigma$  significance or greater in addition to excess short-term variability in the time-series data were flagged as containing possible GRB candidates. This search yielded five additional events that could be confirmed as GRBs by *Ulysses* and/or KONUS detections. There were no other obvious GRB-like events that we could not identify as coming from previously known X-ray sources.

GRB candidate 960529 (Fig. 6b) was detected in two SSCs over two consecutive dwells, yielding four position determinations. The two smallest boxes are plotted in Figure 6b; the largest two are consistent with the intersection of these two. This event was detected by KONUS, but not by *Ulysses*, rendering an IPN annulus impossible to calculate. Both the ASM and KONUS observed three successive peaks, lasting a total of  $\sim 200$  s, but KONUS detected no emission above 50 keV (P. Butterworth 1997, private communication). It is therefore possible that this event was not a GRB but was a series of hard flares from an unknown X-ray source.

GRB 960727 (Fig. 6c) and GRB 961002 (Fig. 6d) were bright events, but both were seen in only one ASM SSC. However, they were both detected by KONUS and *Ulysses*, so annuli could be calculated that reduced the lengths of the error boxes to  $1.4'$  and  $2.1'$ , respectively. GRB 961029 (Fig. 6f) was seen as an abrupt rise in the last few seconds of a single-camera ASM observation, so despite reaching a peak flux of  $\sim 120$  mCrab,

the ASM measured only a total of 289 counts from this GRB. GRB 961230 (Fig. 6g) was also weak (see Table 7), but was detected in two cameras. Neither GRB 961029 nor GRB 961230 was detected by more than one IPN instrument, so triangulation annuli were impossible to calculate in these cases.

Thirdly, as of May 1997, we began searching for GRB events in the real-time ASM data. We first developed software to respond directly to the GRB alerts released by the BATSE team over the Gamma-ray burst Coordinate Network (GCN). The ASM observing plan cannot be changed in response to alerts, but on occasion the ASM FOV will overlap with a BATSE GRB error circle at or shortly after the trigger time. GRBs have been observed by BATSE to last hundreds of seconds, often with multiple peaks (Meegan et al. 1996), and there is evidence that GRBs last longer at lower energies than at higher energies (Fenimore et al. 1995; Piro et al. 1998). Since the ASM rotates every 90 s, a rotation may put the FOV of an SSC over a burst which is in progress.

We compare the BATSE information for each new trigger with the planned observing schedule for the ASM and to alert us if the ASM is scheduled to scan over the BATSE error circle within 1000 s from the time of trigger. This program has led to the detection of five GRBs as of this writing, and the resulting ASM positions were disseminated to the community within 2–12 h from the events, enabling rapid follow-up by other observers. The positions reported here represent refinements that supersede any GRB positions previously reported in IAU or GCN Circulars by the ASM team. However, unless stated explicitly below, these positions differ from the initial error boxes reported in the Circulars by no more than an arcminute.

GRB 970815 (Fig. 6h) had multiple peaks in its light curve, and it was located such that it was detected in a single-SSC during a single 90-s dwell (Smith et al. 1997). During the next dwell, it became much brighter while it was observed with both

TABLE 6  
DIMENSIONS OF IPN ANNULI

Date of GRB (yymmdd)	Instruments <sup>a</sup>	R.A. of Center (J2000)	Decl. of Center (J2000)	3 - $\sigma$ Full-width (Arcmin)	Radius (Degrees)
960416	ub	10h09m15.65s	+67°07'36.8''	23.9	25.706
960727	uk	10h37m45.44s	+42°05'13.3''	1.4	82.222
961002	uk	23h30m18.78s	-33°07'44.4''	2.1	81.847
961019	ub	23h41m20.75s	-31°52'58.3''	11.0	48.530
970815	ub	10h38m36.27s	+20°33'43.9''	2.8	68.519
970828	ub	10h46m12.46s	+19°10'18.6''	1.1	83.514
971214	ub	11h32m40.33s	+11°03'06.3''	13.2	54.331
980703	ub	22h06m35.40s	-9°03'55.7''	13.5	33.132
981220	uk	23h09m29.47s	+7°20'04.3''	0.8	67.142

<sup>a</sup>u - *Ulysses*; b - BATSE; k - KONUS

SSCs 1 and 2. As the event faded during a third dwell, the source location was less than a degree from the edge of the FOV of SSC 1 (and outside the FOV of SSC 2). This location is outside the region of the FOV considered in the present analysis, and a reliable position could therefore not be obtained from this dwell. As with GRB candidate 960529, only the two smallest error boxes are shown in Figure 6h. This GRB was also seen by both BATSE and *Ulysses*, and an IPN annulus confirms the ASM position. Three days after the GRB event, a weak X-ray source with constant intensity near the ASM position was seen by *ASCA* (Murakami et al. 1997a, included in Fig. 6h); its relation to GRB 970815 remains uncertain.

GRB 970828 (Fig. 6i) was localized in two SSCs, and its location was published within two hours of the onset of the event (Remillard et al. 1997). The PCA on *RXTE* slewed to observe the fading X-ray flux within 3.6 h, confirming the ASM position (Marshall, Cannizzo, & Corbet 1997). This PCA observation remains the fastest capture of a GRB afterglow at X-ray energies.

An IPN annulus based on BATSE and *Ulysses* detections was made available  $\sim 1$  d after the ASM report (Hurley et al. 1997). A fading X-ray source was observed with *ASCA* over the interval of 1.2 to 2.1 days after the burst trigger (Murakami et al. 1997b). Later ROSAT observations narrowed the position to within a radius of 10'' (Greiner et al. 1997). Optical and radio instruments observed this location within 4 h of the trigger time, but despite intense monitoring over the following weeks, no counterpart was seen at wavelengths longer than X-rays (Groot et al. 1998).

GRB 971024 (Figure 6j) was detected in two cameras, but the event proved to be extremely weak in the ASM energy band. Due to its position near the edge of the field of view of SSC 2, only 159 counts were detected. The position analysis described above indicates that positions for detections this weak are unreliable, so we do not report an error box from this SSC. The

error box derived from the detection of GRB 971024 in SSC 1 is shown in Figure 6j. Because of the extremely large error region, very little follow-up was performed. No candidate counterpart was reported.

GRB 971214 (Fig. 6k) was detected by SSC 3 within a single dwell. We reported a line of position via the GCN about 2.3 h after the event. This GRB was also detected with BATSE and *Ulysses*, and the resulting IPN annulus, reported two days later, was 7.9' in width (Kippen et al. 1997). The error box reported here is smaller in area than the initial ASM position by about a factor of three. This burst was also detected simultaneously and independently in the Wide-Field Camera of *BeppoSAX*, generating a 99% confidence error circle 3.9' in radius (Heise et al. 1997). This region was further reduced through pointings by the Narrow-Field Instruments (NFI), which localized a fading X-ray counterpart to 1' (Antonelli et al. 1997). The two error circles are shown in Figure 6k. A fading optical source was quickly identified (Halpern et al. 1997), and later observations indicated that the host galaxy candidate had a redshift of  $z = 3.42$  (Kulkarni et al. 1998a).

GRB 980703 (Figure 6l) was a bright burst, the onset of which was seen in two SSCs simultaneously. The ASM position was first reported  $\sim 12$  h after the event (Levine, Morgan, & Munro 1998). Observations of a region centered on the ASM localization with the *BeppoSAX* NFI at 22 h after the BATSE trigger were able to localize a fading X-ray source to within a circle of 50'' radius (Galama et al. 1998a). An IPN annulus 18.4' in width was made available within 3 d (Hurley & Kouveliotou 1998). The final IPN annulus reported here is 13.5' wide; it is consistent with the ASM and *BeppoSAX* measurements. Radio and optical observers were also able to identify counterparts (Frail et al. 1998). Later spectroscopy revealed a redshift of  $z = 0.9653 \pm 0.0007$  (Djorgovski et al. 1998), the third cosmological redshift to be measured for a GRB source.

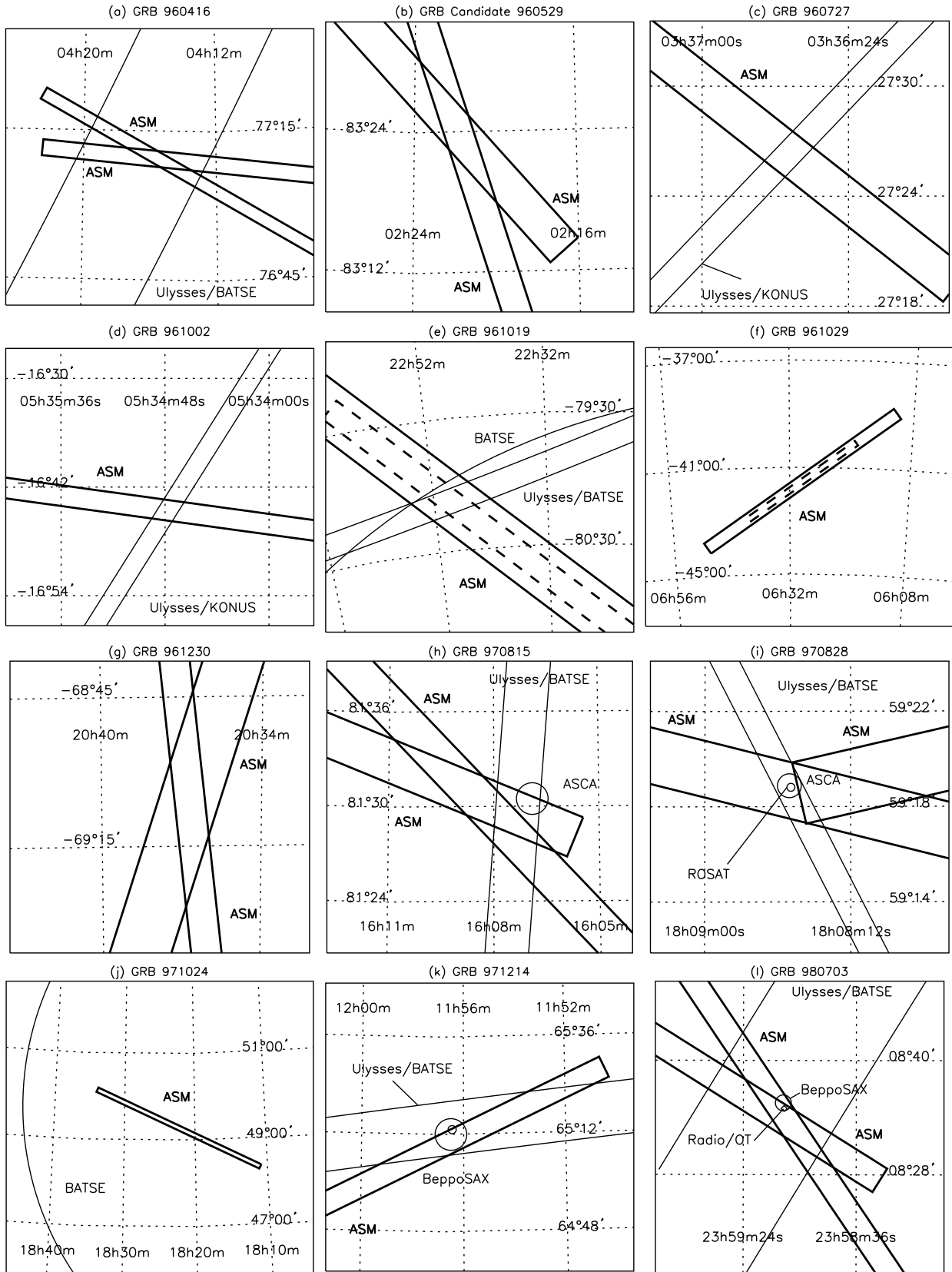


Fig. 6 – The ASM localizations of 12 gamma-ray bursts, shown with position information from other satellites when available. Each frame is mapped at a different scale. ASM (dark lines) and BATSE locations are given at 90% confidence, while IPN annuli are  $3\sigma$ . In cases of dim GRBs, boxes at 68% confidence are also plotted as dashed outlines. Positions and sizes of the 90% regions are given in Tables 2–4, while references to the other instruments are given in the text and in Tables 5–6.

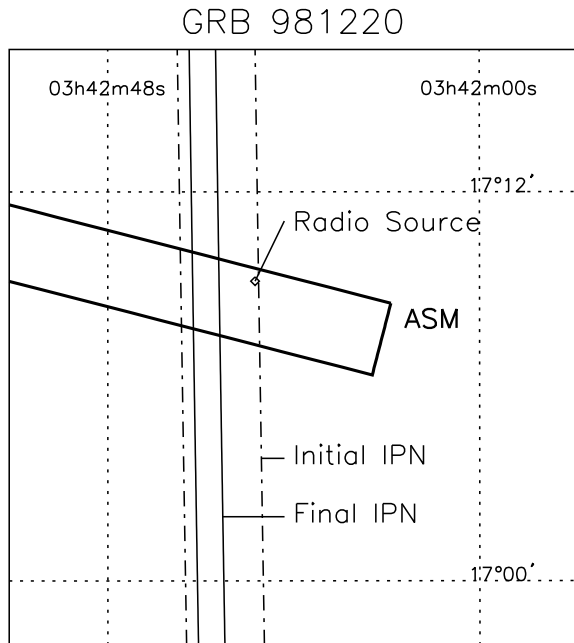


Fig. 7 – The ASM localization of GRB 981220, shown with two IPN annuli constructed by triangulation of burst arrival times at *Ulysses* and *KONUS/WIND*. The radio source at  $\alpha = 03\text{h}42\text{m}28.98\text{s} \pm 0.07\text{s}$ ,  $\delta = +17^\circ 09' 14.7'' \pm 1.6''$  (J2000) was discovered by Galama et al. (1998) and found to be highly variable by Frail & Kulkarni (1998). The final IPN annulus reported here (see Table 6) excludes this radio source as a counterpart to GRB 981220, and further monitoring with the VLA shows behavior inconsistent with that of other GRB afterglow at radio wavelengths (Frail, Kulkarni, & Taylor 1999).

Fourthly, in September of 1997, we established a “self-trigger” system, in which the incoming time-series data is checked for excess variability using the same criteria developed during the archival search described above. Dwells with significant non-linear time series sequences are flagged as possible GRB events. If the standard cross-correlation analysis also reports a possible new source detection at better than  $5\sigma$ , an email alert is distributed. If BATSE and/or *BeppoSAX* data indicate that a GRB was active during the time of the dwell, the significance limit is lowered to  $3\sigma$ , to ensure that a dim GRB does not slip through the system. This system has detected one GRB to date that was not also detected by BATSE.

GRB 981220 (Figure 7) was detected by SSC 2 during a single dwell, and an alert was distributed 32 h after the initial event. An IPN annulus  $2.4'$  wide using *Ulysses* and *KONUS* detections was rapidly calculated (Hurley et al. 1998). Although no optical transients were reported, a rapidly varying radio source was discovered within the ASM/IPN error box and attributed to GRB 981220 (Galama et al. 1998b; Frail & Kulkarni 1998). The final IPN annulus reported in Table 6 is  $0.8'$  wide and excludes this radio source as a counterpart to GRB 981220. Further monitoring with the VLA has shown that the behavior of this source’s light curve does not resemble that of other GRB afterglows (Frail, Kulkarni, & Taylor 1999). This radio source is therefore most likely unrelated to GRB 981220. The nature and characteristics of any afterglow from GRB 981220 remain unknown at this time.

Seven detections of five of these thirteen bursts yielded numbers of counts low enough for the chance that each of the de-

rived positions is spurious to be  $\geq 7\%$ . The probabilities of spurious detections in each coordinate as predicted by Equation 1 are given in Table 7 for all ASM GRB detections. Three weak bursts, GRB 961019 (Fig. 6e), GRB 971024 (Fig. 6j), and GRB 971214 (Fig. 6k), have positions derived from BATSE, IPN, or *BeppoSAX* which confirm the ASM positions. In the case of GRB 961019 (Fig. 6e), the IPN annulus significantly reduces the size of the error box. In the case of GRB 961230 (Fig. 6g), the weak ASM positions confirm each other (the probability that two spurious boxes overlap by chance is less than  $10^{-3}$ ), but there are no independently derived positions to compare with the ASM error region for GRB 961029 (Fig. 6f).

Three further GRBs (GRB 961216, GRB 971216 and GRB 981005) had BATSE positions that were consistent with the ASM FOV at the time of trigger, and ASM analysis indicated the presence of uncatalogued X-ray source candidates in the FOV of at least one SSC. In the case of GRB 961216, a  $\sim 4\sigma$  peak was detected less than a degree from the edge of the FOV of a single SSC. This position lies outside the region of the FOV included in the present analysis, so we do not report it here. Observations at the times of GRB 971216 and GRB 981005 were more complex. The highest peaks in the cross-correlation maps derived from SSCs 1 and 2 had low significance ( $\sim 2\text{--}4\sigma$ ), fell below the 200-count lower limit for reliability, and mapped to inconsistent celestial locations. We are therefore unable to report reliable detections for either of these bursts. Furthermore, we cannot provide useful upper limits for the X-ray fluxes from these GRBs, since it is possible that the actual GRB sources were located outside the FOV of the ASM during all of these observations.

Although we know of no other bright, burst-like events in the ASM database that we cannot identify, it is possible that the ASM has detected GRBs other than the ones reported here. Our understanding of how to distinguish real short-lived X-ray events from solar- or particle-induced events has improved since the archival search described above was completed. The difficulty in identifying real events in the archival search led us to exclude approximately one-third of the data from consideration. We may also miss GRBs in the real-time search, if the telemetry stream from the satellite is interrupted by internet or server outages on the ground, or if the packets are received out of order. These problems are corrected in production data, which are available  $\sim 1\text{--}4$  days after the observations, but these data are not currently being searched for GRBs. Projects to reprocess the archival data and utilize the production data to create a complete ASM GRB catalog are planned.

We argue above that we have identified nearly all the GRBs above a certain threshold in the  $\sim 2 \times 10^7$  sr of sky coverage examined via the searches reported here (roughly 60% of the first three years of ASM observations). The observed burst rate is therefore  $7 \times 10^{-7} \text{ s}^{-1} \text{ sr}^{-1}$ . The BATSE 4B catalog records a full-sky burst rate of  $1.7 \times 10^{-6} \text{ s}^{-1} \text{ sr}^{-1}$  when corrected for the BATSE sky exposure (Paciesas et al. 1999), although this rate ignores non-triggered GRBs such as those found by Komers et al. (1997). If the ASM can detect all the BATSE GRBs that appear in its FOV, we would expect to find 33 GRBs in our subset of the ASM database.

Clearly, the simple assumptions of this calculation of the rate of ASM-detectable GRBs are inadequate. In section 2.3, we show that the ASM is less sensitive to a source closer to the edge of the FOV than to a source of identical brightness at the center of the FOV. The calculation of the ASM sky coverage

TABLE 7  
PROBABILITY OF MISIDENTIFYING WEAK BURSTS

Date of GRB (yyymmdd)	SSC Number	Number of counts	Chance of spurious detection in $\phi$ (%)	Chance of spurious detection in $\theta$ (%)
960416	1	997	2	3
960416	2	1424	4	2
960529	1	1035	1	3
960529	1	1043	1	3
960529	2	2223	3	2
960727	2	1899	3	2
961002	2	1498	4	2
961019	2	297	23	38
961029	2	289	24	41
961230	1	329	8	12
961230	2	386	14	19
970815	2	1060	4	3
970815	1	4843	1	2
970815	2	3769	3	1
970828	1	1348	1	3
970828	2	1230	4	3
971024	1	303	10	14
971214	3	662	6	13
980703	1	1539	1	3
980703	2	1622	3	2
981220	2	2236	3	2

is therefore overestimated. Also, it is not clear how the characteristics of the BATSE GRB population extrapolate to X-ray energies. All of the bursts reported here lasted more than ten seconds, while the BATSE duration distribution includes a significant population below 1 s (Paciesas et al. 1999). Although the ASM has detected short bursts from Soft Gamma Repeaters (Smith, Bradt, & Levine 1999), we have found no other short, bright events that might be GRBs. A thorough treatment of the burst rate is beyond the scope of this paper, and we defer it to a later investigation.

#### 4. SUMMARY

This paper describes an empirical method to characterize the error distribution of the ASM source-localization analysis. We used  $\sim 14,000$  observations of sources at random positions in the central  $9.2^\circ \times 90^\circ$  region of the FOV. An ASM error box derived from a single SSC detection takes the shape of a long, thin rectangle. We found that the accuracy (at 95% confidence) of the derived positions in the short direction ( $\phi$ ) is fairly steady at  $\pm 1.2'$  ( $\pm 1.9'$  in SSC 3) for bright sources, but increases rapidly as the detected number of counts falls below  $\sim 700$ . The error in the long direction ( $\theta$ ) does not level off as dramatically for bright sources, but decreases with increasing source brightness, ranging from about  $\pm 1.5^\circ$  to about  $\pm 12'$  for observations yielding  $\gtrsim 700$  counts. The chance that an error box represents a spurious detection rises rapidly for detections yielding  $\lesssim 700$  counts, and detections with less than 200 counts (300 counts in SSC 3) do not yield reliable positions.

We apply this method to the localization of GRBs detected serendipitously by the ASM. Through realtime monitoring and

archival searches, we have localized thirteen GRBs detected in the first three years of ASM observations. This list is most likely not complete, because it has not yet been possible to thoroughly search the entire database of ASM production data. The ASM is not designed to distinguish between GRBs and X-ray bursts; we have relied on confirmations from other instruments to identify these events. Nevertheless, we found no unconfirmed burst-like events that we could not identify with known X-ray sources. Of the thirteen GRBs presented here, six were observed in two SSCs, so the GRBs were localized within diamond-shaped error boxes a few arcminutes on a side. The error boxes from each of five further single-SSC detections were combined with an IPN annulus to obtain joint error boxes of a few arcminutes in each of two dimensions. These error boxes are useful for follow-up studies of GRBs at other wavelengths.

Rapid analysis of ASM data has led to several successful and provocative discoveries. The initial ASM position of GRB 970828 was released within 2 h of the burst event, enabling X-ray, optical and radio observations to be performed within 3.6 h of the initial trigger. While a fading X-ray counterpart was detected with *ASCA* and *ROSAT*, no counterparts were seen at longer wavelengths to a limiting magnitude of  $\sim 24$  (Groot et al. 1998). The thorough coverage in optical and radio bands of this well-constrained area established convincingly that GRB afterglows span a wide range of intensities. Groot et al. (1998) suggest two possible explanations for the faintness of any optical counterpart: beaming in the blast wave could be directing the emission away from the Earth, or strong extinction enhanced by the unknown redshift, could be reducing the apparent magnitude of the source below detectable limits. This latter hypothesis might imply that GRBs occur in star-forming

regions, as predicted by the “hypernovae” class of GRB models (Paczynski 1998).

In the case of GRB 980703, the ASM position was reported within 12 h of the burst event (Levine et al. 1998), which led to the rapid identification of a fading optical counterpart as well as a rapidly varying radio counterpart (Frail et al. 1998). Further spectroscopic observations of the fading optical transient led to the measurement of a redshift of  $z = 0.9653 \pm 0.0007$  (Djorgovski et al. 1998); the third cosmological redshift ever

measured for a GRB.

The authors wish to thank Saul Rappaport and John Doty for helpful discussions, as well as Scott Barthelmy for his inestimable service in providing the GCN. KH is grateful for support under JPL Contract 958056 for Ulysses operations, and to NASA Grant NAG 5 3811 for support of the IPN. Support for this work was provided in part by NASA Contract NAS5-30612.

#### REFERENCES

- Antonelli, A., Butler, R., Piro, L., Celidonio, G., Coletta, A., Tesseri, A., & De Libero, C. 1997, *IAU Circ.*, 6792
- Bloom, J., Djorgovski, S., Kulkarni, S., Brauher, J., Frail, D., Goodrich, R., & Chaffee, F. 1999, *GCN Circ.* 196
- Briggs, M., et al. 1999, *ApJS*, submitted (astro-ph/9901111)
- Costa, E., et al. 1997a, *IAU Circ.*, 6572
- Costa, E., et al. 1997b, *IAU Circ.*, 6576
- Djorgovski, S., Kulkarni, S., Bloom, J., Goodrich, R., Frail, D., Piro, L., & Palazzi, E. 1998, *ApJ*, 508, L17
- Djorgovski, S., Kulkarni, S., Bloom, J., Frail, D., Chaffee, F., & Goodrich, R. 1999, *GCN Circ.* 189
- Fenimore, E., in’t Zand, J., Norris, J., Bonnell, J., & Nemiroff, R. 1995, *ApJ*, 448, L101
- Fishman, G., & Meegan, C. 1995, *ARA&A*, 33, 415
- Frail, D., Halpern, J., Bloom, J., Kulkarni, S., & Djorgovski, S. 1998, *GCN Circ.* 128
- Frail, D., & Kulkarni, S. 1998, *GCN Circ.* 170
- Frail, D., Kulkarni, S., & Taylor, G. 1999, *GCN Circ.* 269
- Galama, T., van Paradijs, J., Antonelli, L., Vreeswijk, P., Kouveliotou, C., Torroni, V., & Pastor, C. 1998a, *GCN Circ.* 127
- Galama, T., Vreeswijk, P., van Paradijs, J., Kouveliotou, C., Strom, R., & de Bruyn, G. 1998b, *GCN Circ.* 168
- Greiner, J., Schwarz, R., Groot, P., & Galama, T. 1997, *IAU Circ.*, 6757
- Groot, P., et al. 1998, *ApJ*, 493, L27
- Halpern, J., Thorstensen, J., Helfand, D., & Costa, E. 1997, *IAU Circ.*, 6788
- Heise, J., et al. 1997, *IAU Circ.*, 6787
- Hjorth, J., et al. 1999, *GCN Circ.* 219
- Hurley, K., Kouveliotou, C., Fishman, G., Meegan, C., Connaughton, V., & van Paradijs, J. 1997, *IAU Circ.*, 6728
- Hurley, K., & Kouveliotou, C. 1998, *GCN Circ.* 125
- Hurley, K., Cline, T., Mazets, E., Golenetskii, S., & Smith, D. A. 1998, *GCN Circ.* 160
- Hurley, K., et al. 1999a, *A&AS*, 120, 408
- Hurley, K., et al. 1999b, *A&AS*, in press (astro-ph/9812024)
- Jager, R., et al. 1998, *A&A*, 125, 557
- Kelson, D., Illingworth, G., Franx, M., Magee, D., & van Dokkum, P. 1999, *IAU Circ.*, 7096
- Kippen, R., Woods, P., Connaughton, V., Smith, D., Levine, A., Remillard, R., & Hurley, K. 1997, *IAU Circ.*, 6789
- Kommers, J., Lewin, W., Kouveliotou, C., van Paradijs, J., Pendleton, G., Meegan, C., & Fishman, G. 1997, *ApJ*, 491, 704
- Kulkarni, S., et al. 1998a, *Nature*, 393, 35
- Kulkarni, S., et al. 1998b, *Nature*, 395, 663
- Levine, A., Bradt, H., Cui, W., Jernigan, J., Morgan, E., Remillard, R., Shirey, R., & Smith, D. 1996, *ApJ*, 469, L33
- Levine, A., Morgan, E., & Muno, M. 1998, *IAU Circ.*, 6966
- Marshall, F., Cannizzo, J., & Corbet, R. 1997, *IAU Circ.*, 6727
- Meegan, C. et al. 1996, *ApJS*, 106, 65
- Metzger, M., Cohen, J., Chaffee, F., & Blandford, R. 1997, *IAU Circ.*, 6676
- Murakami, T., Ueda, Y., Ishida, M., Fujimoto, R., Yoshida, A., & Kawai, N. 1997a, *IAU Circ.*, 6722
- Murakami, T., Ueda, Y., Yoshida, A., Kawai, N., Marshall, F., Corbet, R., & Takeshima, T. 1997b, *IAU Circ.*, 6732
- Paciesas, W., et al. 1999, *ApJS*, in press (astro-ph/9903205)
- Paczynski, B. 1998, *ApJ*, 494, L45
- Piro, L., et al. 1998, *A&A*, 329, 906
- Rees, M. & Mészáros, P. 1992, *MNRAS*, 258, P41
- Remillard, R., Wood, A., Smith, D., & Levine, A. 1997, *IAU Circ.*, 6726
- Smith, D., Bradt, H., & Levine, A. 1999, *ApJ*, 519, L150
- Smith, D., Levine, A., Morgan, E., & Wood, A. 1997, *IAU Circ.*, 6718
- Takeshima, T., et al. 1998, in *Gamma-Ray Bursts: 4th Huntsville Symposium*, eds. C. A. Meegan, R. D. Preece, & T. M. Koshut, (New York: American Institute of Physics), 414
- van Paradijs, et al. 1997, *Nature*, 386, 686
- Wijers, R. & Galama, T. 1998, *ApJ*, submitted (astro-ph/9805341)